

This work was written as part of one of the author's official duties as an Employee of the United States Government and is therefore a work of the United States Government. In accordance with 17 U.S.C. 105, no copyright protection is available for such works under U.S. Law.

Public Domain Mark 1.0

<https://creativecommons.org/publicdomain/mark/1.0/>

Access to this work was provided by the University of Maryland, Baltimore County (UMBC) ScholarWorks@UMBC digital repository on the Maryland Shared Open Access (MD-SOAR) platform.

Please provide feedback

Please support the ScholarWorks@UMBC repository by emailing scholarworks-group@umbc.edu and telling us what having access to this work means to you and why it's important to you. Thank you.

Complex variations of X-ray polarization in the X-ray pulsar LS V +44 17/RX J0440.9+4431

Victor Doroshenko¹, Juri Poutanen², Jeremy Heyl³, Sergey S. Tsygankov², Ilaria Caiazzo⁴, Roberto Turolla^{5,6},
Alexandra Veledina^{2,7}, Martin C. Weisskopf⁸, Sofia V. Forsblom², Denis González-Caniulef⁹, Vladislav Loktev²,
Christian Malacaria¹⁰, Alexander A. Mushtukov¹¹, Valery F. Suleimanov¹, Alexander A. Lutovinov¹²,
Ilya A. Mereminskiy¹², Sergey V. Molkov¹², Alexander Salganik^{13,12}, Andrea Santangelo¹, Andrei V. Berdyugin²,
Vadim Kravtsov², Anagha P. Nitindala², Iván Agudo¹⁴, Lucio A. Antonelli^{15,16}, Matteo Bachetti¹⁷, Luca Baldini^{18,19},
Wayne H. Baumgartner⁸, Ronaldo Bellazzini¹⁸, Stefano Bianchi²⁰, Stephen D. Bongiorno⁸, Raffaella Bonino^{21,22},
Alessandro Brez¹⁸, Niccolò Bucciantini^{23,24,25}, Fiamma Capitanio²⁹, Simone Castellano¹⁸, Elisabetta Cavazzuti²⁶,
Chien-Ting Chen²⁷, Stefano Ciprini^{28,16}, Enrico Costa²⁹, Alessandra De Rosa²⁹, Ettore Del Monte²⁹, Laura Di Gesu²⁶,
Niccolò Di Lalla³⁰, Alessandro Di Marco²⁹, Immacolata Donnarumma²⁶, Michal Dovčiak³¹, Steven R. Ehlert⁸,
Teruaki Enoto³², Yuri Evangelista²⁹, Sergio Fabiani²⁹, Riccardo Ferrazzoli²⁹, Javier A. García³³, Shuichi Gunji³⁴,
Kiyoshi Hayashida^{35*}, Wataru Iwakiri³⁶, Svetlana G. Jorstad^{37,13}, Philip Kaaret⁸, Vladimir Karas³¹, Fabian Kislak³⁸,
Takao Kitaguchi³², Jeffery J. Kolodziejczak⁸, Henric Krawczynski³⁹, Fabio La Monaca²⁹, Luca Latronico²¹,
Ioannis Lioudakis⁴⁰, Simone Maldera²¹, Alberto Manfreda⁴¹, Frédéric Marin⁴², Andrea Marinucci²⁶, Alan P. Marscher³⁷,
Herman L. Marshall⁴³, Francesco Massaro^{21,22}, Giorgio Matt²⁰, Ikuyuki Mitsuishi⁴⁴, Tsunefumi Mizuno⁴⁵,
Fabio Muleri²⁹, Michela Negro^{46,47,48}, Chi-Yung Ng⁴⁹, Stephen L. O'Dell⁸, Nicola Omodei³⁰, Chiara Oppedisano²¹,
Alessandro Papitto¹⁵, George G. Pavlov⁵⁰, Abel L. Peirson³⁰, Matteo Perri^{16,15}, Melissa Pesce-Rollins¹⁸,
Pierre-Olivier Petrucci⁵¹, Maura Pilia¹⁷, Andrea Possenti¹⁷, Simonetta Puccetti¹⁶, Brian D. Ramsey⁸, John Rankin²⁹,
Ajay Ratheesh²⁹, Oliver J. Roberts²⁷, Roger W. Romani³⁰, Carmelo Sgrò¹⁸, Patrick Slane⁵², Paolo Soffitta²⁹,
Gloria Spandre¹⁸, Douglas A. Swartz²⁷, Toru Tamagawa³², Fabrizio Tavecchio⁵³, Roberto Taverna⁵, Yuzuru Tawara⁴⁴,
Allyn F. Tennant⁸, Nicholas E. Thomas⁸, Francesco Tombesi^{54,28,55}, Alessio Trois¹⁷, Jacco Vink⁵⁶, Kinwah Wu⁶,
Fei Xie^{57,29}, and Silvia Zane⁶

(Affiliations can be found after the references)

June 6, 2023

ABSTRACT

We report on IXPE observations of the Be-transient X-ray pulsar LS V +44 17/RX J0440.9+4431 at two luminosity levels during the giant outburst in January–February 2023. Considering the observed spectral variability and changes in the pulse profiles, the source was likely caught in super- and sub-critical states with significantly different emission region geometry, associated with the presence of accretion columns and hot spots, respectively. We focus here on the pulse-phase resolved polarimetric analysis and find that the observed dependencies of the polarization degree and polarization angle (PA) on pulse phase are indeed drastically different for the two observations. The observed differences, if interpreted within the framework of the rotating vector model (RVM), imply dramatic variations of the spin axis inclination and the position angle and the magnetic colatitude by tens of degrees within just a few days separating the observations. We suggest that the apparent changes in the observed PA phase dependence are predominantly related to the presence of a polarized unpulsed component in addition to the polarized radiation associated with the pulsar itself. We show that the observed PA phase dependence in both observations can then be explained with a single set of RVM parameters defining the pulsar's geometry. We also suggest that the additional polarized component is likely produced by scattering of the pulsar radiation off the equatorial disk wind.

Key words. accretion, accretion disks – magnetic fields – pulsars: individual: RX J0440.9+4431 – stars: neutron – X-rays: binaries

1. Introduction

The Be/X-ray binary (BeXRB) LS V +44 17/RX J0440.9+4431 was discovered and identified as candidate X-ray binary at ~ 3.2 kpc in the ROSAT survey (Motch et al. 1997). The discovery of hard X-ray emission and pulsations with a period of about 206 s confirmed the source being an X-ray pulsar (XRP, Reig & Roche 1999). The properties of the optical counterpart were investigated in detail by Reig et al. (2005) who classified

it as Be star of class B0.2V and reported on brightness and H α line profile variability typical for this class of sources. Reig et al. (2005) also estimated the distance to the source at around 3.3 kpc, which, however, has been recently revised to 2.4 ± 0.1 kpc based on *Gaia* DR3 data (Bailer-Jones et al. 2021).

Properties of the binary remain relatively unexplored in the X-ray band as only a handful of relatively faint Type I outbursts typical for Be X-ray binaries were observed up to now (Morii et al. 2010; Tsygankov et al. 2012; Ferrigno et al. 2013). Besides the outburst activity typical for BeXRBs, LS V +44 17 is also known

* Deceased

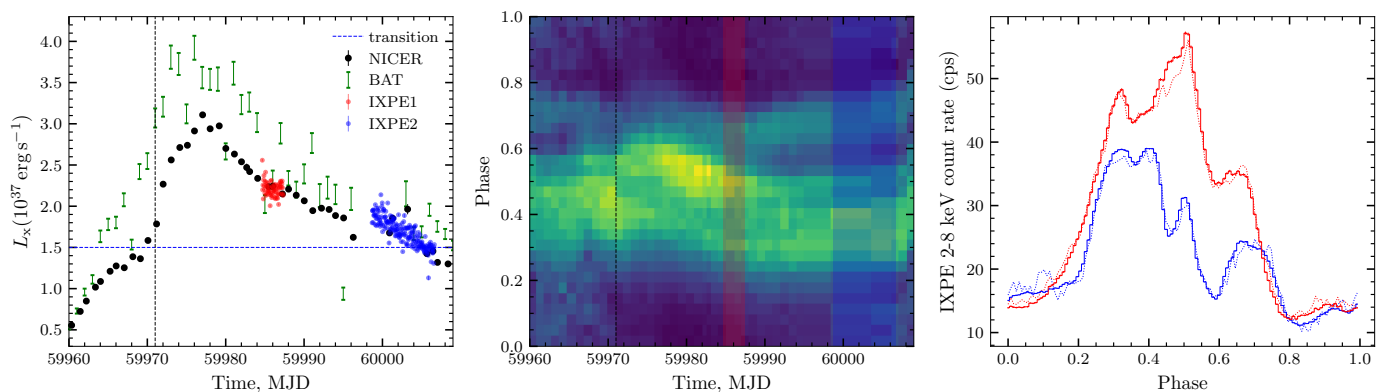


Fig. 1. *Left:* Light curve of the 2023 outburst of RX J0440.9+4431 as observed by facilities indicated in the legend and described in the main text. The vertical dashed line marks the probable date for the transition to a super-critical regime, while the horizontal dashed line marks the approximate luminosity level at the transition. *Middle:* overall evolution of the pulse profiles during the outburst as observed by NICER (slices in vertical direction correspond to pulse profiles in individual NICER observations), the shaded strips mark times of IXPE observations and the vertical dashed line is the same as in the left panel. *Right:* Pulse profiles in the 2–8 keV band observed by IXPE in two observations (histogram) and NICER during the same period (dotted line, scaled to match IXPE count rate).

for being one of the few systems in which accretion continues also in quiescence, in this case at the X-ray luminosity $L_X \sim (1.5 - 4) \times 10^{34} \text{ erg s}^{-1}$ (Reig & Roche 1999; La Palombara et al. 2012). We note that considering the observed spin period and luminosity, the accretion in quiescence is likely powered by a cold non-ionized disk (Tsygankov et al. 2017), although wind accretion cannot be excluded.

The transient was mainly active in 2010 and 2011 (Morii et al. 2010; Finger & Camero-Arranz 2010; Tsygankov et al. 2012; Ferrigno et al. 2013) reaching peak luminosities of $(1 - 5) \times 10^{36} \text{ erg s}^{-1}$ (here and below we adopt the revised distance estimate of 2.4 kpc). Based on observations during this period a tentative orbital period of $\sim 150 \text{ d}$ and presence of a cyclotron line at $\sim 30 \text{ keV}$, implying a magnetic field of $B \sim 3 \times 10^{12} \text{ G}$, have been reported by Tsygankov et al. (2012). No evidence for such a feature was, however, found by Ferrigno et al. (2013) using the same data and observations of the 2011 outburst. The reported pulse profiles were relatively simple and almost sine-like throughout the 0.3–60 keV energy range, although some luminosity-dependent structures can be identified in the 3–15 keV range where counting statistics is highest (Tsygankov et al. 2012). In particular, a relatively sharp dip following the main peak also reported by Usui et al. (2012) can be noted. This has been interpreted as obscuration of the emission region by the accretion stream. The relatively low observed luminosity and a rather simple pulse profile shape indicate that during these observations the source likely resided in the sub-critical accretion regime, when the emission came directly from a hotspot and not from an accretion column expected to arise at higher luminosities (Basko & Sunyaev 1976). On the other hand, Ferrigno et al. (2013) investigated in detail the evolution of the spectral energy distribution with luminosity and concluded that the spectral curvature observed at the highest luminosities may be attributed to the transition to a radiative-pressure-dominated accretion regime and the onset of an accretion column at $L_X \sim 2 \times 10^{36} \text{ erg s}^{-1}$, which they argued is consistent with theoretic expectations assuming the magnetic field strength estimated from the observed cyclotron line energy. We conclude thus that there are no solid constraints on the magnetic field nor the emission region geometry for this object.

Most recently RX J0440.9+4431 became active starting in December 2022 (Nakajima et al. 2022) when another Type I outburst similar to those in 2010–2011 was observed. The source

then entered a giant outburst in January–February 2023 peaking at a luminosity of $\sim 4 \times 10^{37} \text{ erg s}^{-1}$ (Pal et al. 2023; Salganik et al. 2023b), i.e. several times brighter than previously observed. Extensive monitoring by several facilities including NuSTAR and NICER allowed Coley et al. (2023) and Salganik et al. (2023a) to detect transitions in the spectral and timing properties of the source around MJD 59971 and MJD 59995 marked in the left panel of Fig. 1 with the vertical dashed line and interpreted by Salganik et al. (2023a) as marking the transition to super-critical accretion regime and then back. Here we focus on the results obtained with the *Imaging X-ray Polarimeter Explorer* (IXPE, Weisskopf et al. 2022), which observed the source in both states. The launch of IXPE has opened a new observational window in the form of X-ray polarimetry which, in the case of accreting XRPs can be used to obtain independent constraints on their geometrical parameters through pulse-phase resolved polarimetric analysis which is the main objective of the current work.

The paper is organized as follows. In Section 2, we provide a summary of observations used and briefly discuss the analysis procedures adopted. In Section 3 we discuss IXPE results in more detail and put those in context of the results of outburst monitoring by NICER. We model the data and provide constraints on the pulsar geometry and discuss implications of the obtained results in a broader context in Section 4. We summarize our findings in Section 5.

2. Observations and data analysis

IXPE observed the source twice at a factor of two different flux levels. The first observation with ObsID 02250401 was carried out between MJD 59984.65–59987.40 (132 ks effective exposure, around 3.8 M source counts in the 2–8 keV band in total). The second observation with ObsID 02250501 between MJD 59998.66–60006.66 (373 ks effective exposure with 8.3 M source counts in total). We also used NICER observations complemented with *Fermi*/GBM measurements of source spin frequency (Malacaria et al. 2020) to characterize the evolution of the soft pulse profile shape over the outburst in order to ensure accurate absolute pulse phase alignment of IXPE data. In the following section we briefly describe relevant properties, analysis procedures and the results

Table 1. Pulsar ephemerides for the two IXPE observations.

Parameter	IXPE1	IXPE2
T_0 (MJD)	59984.64718	59998.65768
ν (mHz)	4.8484(8)	4.8670(1)
$\dot{\nu}$ (s ⁻²)	$3(2) \times 10^{-11}$	$1.42(3) \times 10^{-11}$
$\ddot{\nu}$ (s ⁻³)	$-1(2) \times 10^{-16}$	$-8(1) \times 10^{-18}$

Notes. The uncertainties are reported at 1σ confidence level, the reference epoch T_0 is fixed to arrival time of the first pulse.

for each instrument. Finally, we made use of the *Swift*/BAT 15–50 keV light curve.¹

2.1. IXPE

The IXPE is a NASA mission in partnership with the Italian Space Agency launched on 2021 December 9. It consists of three identical grazing incidence telescope/detector modules operating in the 2–8 keV energy band. Each telescope comprises an X-ray mirror assembly and a polarization-sensitive detector unit (DU) equipped with a gas-pixel detector (Soffitta et al. 2021; Baldini et al. 2021) and provides imaging polarimetry with a time resolution better than 10 μ s over the detector-limited field of view of $12.9' \times 12.9'$. A detailed description of the observatory and its performance is given in Weisskopf et al. (2022). The Level 2 data were processed with the IXPEOBSSIM package (Baldini et al. 2022) version 30.2.3² using the Calibration database released on 2022 November 17 (v12). Source photons were collected from a circular region with radius R_{src} of 1.6' centered on the source position determined by fitting a Gaussian function to the raw count map. The background appears to be negligible in both observations (a typical background count rate from a region of the same size in the 2–8 keV band of IXPE is ~ 0.02 count s⁻¹ and the observed source count rate is ≥ 10 count s⁻¹ at all times), and thus its contribution was ignored in the analysis (Di Marco et al. 2023). Taking into account high number of source counts even in individual phase bins and low background level, we employed also no track weighing or acceptance corrections.

For the timing analysis, the photons arrival times were corrected to the Solar system barycenter using the *barycorr* task. No binary correction was done as at the time of writing orbital parameters of the system are still not known. The pulsar ephemerides were then obtained for each of the IXPE observations using the phase-connection technique (Deeter et al. 1981) and are reported in Table 1. The absolute phase alignment between the two IXPE observations was done using the peak at phase around 0.5 which appears to be present throughout most of the outburst as indicated by NICER monitoring and discussed below. The ephemerides were then either used directly to produce pulse profiles or to generate a set of good time interval files (GTI) to define phase intervals for pulse-phase resolved analysis. Using *pcube* routine in IXPEOBSSIM (Baldini et al. 2022) in a broad 2–8 keV band, we extract binned Stokes parameters I , Q , and U (Kislat et al. 2015) taking into the account modulation factor of the instrument. We define normalized Stokes parameters as $q = Q/I$ and $u = U/I$. The polarization degree (PD) and the polarization angle (PA) can be obtained using standard formulae: $\text{PD} = \sqrt{q^2 + u^2}$ and $\text{PA} = \frac{1}{2} \arctan(u/q)$.

¹ <https://swift.gsfc.nasa.gov/results/transients/weak/LSVp4417/>

² <https://github.com/lucabaldini/ixpeobssim>

2.2. NICER

Besides absolute phasing, monitoring of pulse profile shape changes can be also a useful probe for possible changes of the accretion regime associated with the onset of an accretion column (Reig & Nespoli 2013; Wilson-Hodge et al. 2018; Doroshenko et al. 2020), and put the snapshot IXPE observations in a broader context. All available NICER observations were processed using the *nicerl2* task and then light curves in the 1–10, 4–7 and 7–10 keV energy bands were extracted using the *nicerl3-1c* script. The extracted light curves were then corrected to the Solar system barycenter and folded assuming a single phase model based on the spin frequency measurements of the source done by *Fermi*/GBM³ as follows. First, we interpolated raw frequency measurements to obtain a smooth function characterizing the frequency evolution of the source with time. This interpolated function was then used to calculate the absolute phase of each pulse within the period covered by the observations. That is, the arrival time of each subsequent pulse was calculated using the arrival time and local frequency of the previous one (for the first pulse the phase was set arbitrarily). Finally, we calculated a reference epoch and folding frequency for each of the NICER observations using the obtained interpolated functions. The reference phase was selected such that the narrow peak at phase ~ 0.5 visible in both IXPE observations occurs at the same phase also in simultaneous NICER data. The result presented in Fig. 1 exhibits no major regular phase drifts and is consistent with the correlation-based alignment procedure outlined in Doroshenko et al. (2020). We conclude, therefore, that despite uncertainty in orbital parameters of the system and rapid observed spin-up, the observed spin frequency evolution implies that the sharp peak around phase 0.5 is indeed the same feature in both IXPE observations and thus their absolute phase alignment obtained above is indeed correct.

3. Results

Similarly to other accreting pulsars observed by IXPE so far (Doroshenko et al. 2022; Tsygankov et al. 2023; Mushtukov et al. 2023; Malacaria et al. 2023; Forsblom et al. 2023), the average polarization in the 2–8 keV band observed from the source is low. We measure a PD of $4.4\% \pm 0.2\%$ at $\text{PA} = 79^\circ \pm 2^\circ$ in the first, and $\text{PD} = 4.9\% \pm 0.2\%$, $\text{PA} = -59^\circ \pm 2^\circ$ in the second observation, respectively (uncertainties here and throughout the manuscript are reported at 1σ confidence level unless stated otherwise). More interesting is the pulse-phase dependence of the observed polarization properties. As a next step, we conducted, therefore, a phase-resolved polarimetric analysis. The results for both observations are presented in Fig. 2. We also verified that spectro-polarimetric analysis with *xspec* (Arnaud 1996) using a simple absorbed Comptonization model gives consistent results. The motivation for the choice of the binned analysis over spectro-polarimetry is discussed below in Section 4. The polarization is detected with significance exceeding 3σ in 14 out of 16 phase bins in the first observation, and in all 32 phase bins of the second observation. The higher quality of the data in the latter case is related to a significantly longer exposure which allowed us to collect more photons (despite factor of two lower flux) and a higher average PD.

As evident from Fig. 2, both the observed pulse profiles and the polarization properties appear to be drastically different between the two observations. The PD is significantly larger in

³ <https://gammaaray.nsstc.nasa.gov/gbm/science/pulsars/lightcurves/rxj0440.html>

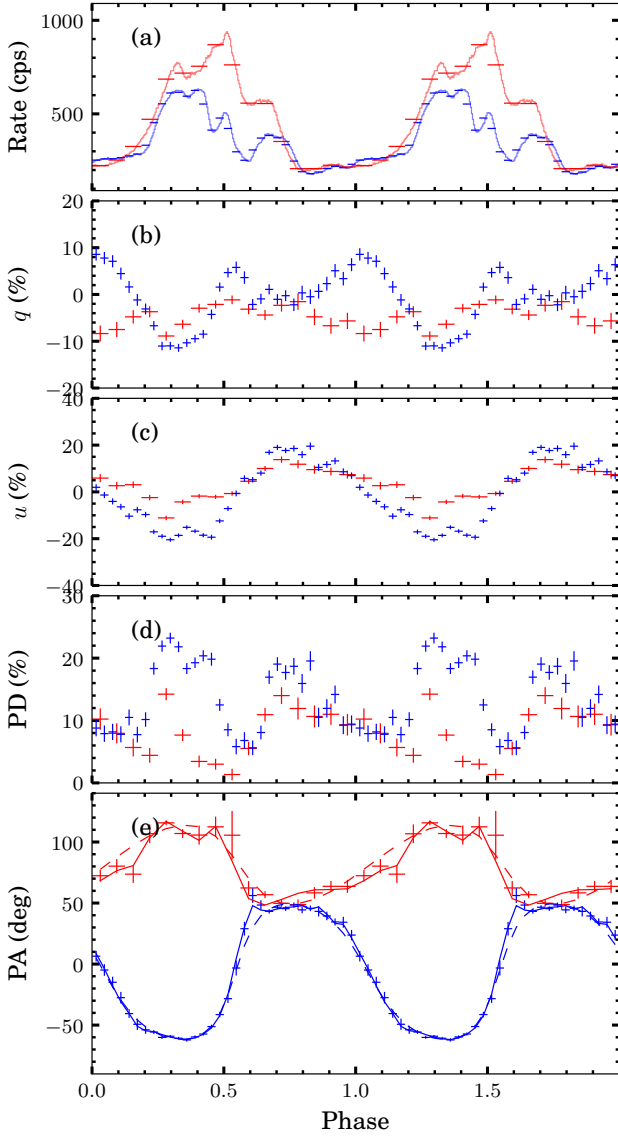


Fig. 2. Pulse phase dependence of the source flux, normalized Stokes parameters $q = Q/I$ and $u = U/I$, PD, and PA for the first (red) and second (blue) IXPE observations. In panel (e), the lines show the RVM best-fit model for each observation individually with no extra components (dashed, Sect. 4.1) and a joint fit including a constant polarization component (solid, Sect. 4.2).

observation 2, reaching 25%, while it remains below 15% in observation 1. The profile of the PD (see Fig. 2d) exhibits similar features such as a peak at phase 0.3 and a secondary broad peak at phase 0.7–0.8, while the third peak of the PD at phase 0.4 present in observation 2 is not present in observation 1. The observed changes in PA phase dependence between the two observations are even more noteworthy. The PA as function of phase not only appears to be in anti-phase in the two observations, but also the amplitude of variations changes by a factor of two. Another important point one could make here is the remarkable comparative simplicity of the PA phase dependence in both observations, especially so in the second one (see Fig. 2e). This can be contrasted to the complex pulse profile that exhibits multiple peaks varying with energy (see Fig. 2a) and also significantly different in the two observations (even if some common features like such as narrow peaks with phase $\sim 0.3, 0.5$ and 0.7 and dips around phases 0.6

and 0.9 can be identified). It is also worth noticing that absolute flux around the pulse minimum remains almost constant whereas the maximum flux changes significantly. As a consequence, the pulsed fraction decreases from $\sim 66\%$ in the first to $\sim 56\%$ in the second observation remaining, however, unusually high (see also Salganik et al. 2023a). On the other hand, the PA exhibits in both cases almost sinusoidal modulation with no extra features despite the statistics being definitively sufficient to detect those.

4. Modeling

The observed dramatic changes in pulse profile shape and polarization properties are, in fact, not totally unexpected given the likely transition to the super-critical accretion regime (Salganik et al. 2023a) and definitively deserve more detailed analysis. Considering the lack of reliable model predictions for the PD, we focus below mainly on the analysis of the PA phase dependence.

4.1. Rotating vector model

The observed remarkably simple evolution of the PA with the pulse phase ϕ observed up to now with IXPE (Doroshenko et al. 2022; Tsygankov et al. 2022, 2023) is likely related to the alignment of the PA to the projection of the magnetic dipole on the sky due to vacuum polarization (Gnedin et al. 1978; Pavlov & Shibanov 1979; Heyl & Shaviv 2000; Doroshenko et al. 2022; González-Caniulef et al. 2023). This allows us to constrain the basic geometry of the pulsar using the rotating vector model (RVM; Radhakrishnan & Cooke 1969; Poutanen 2020):

$$\tan(\chi - \chi_p) = \frac{-\sin \theta \sin[2\pi(\phi - \phi_p)]}{\sin i_p \cos \theta - \cos i_p \sin \theta \cos[2\pi(\phi - \phi_p)]}. \quad (1)$$

Here $\chi(\phi)$ is the prediction of the RVM for the PA, χ_p is the position angle (measured from north to east) of the pulsar angular momentum, $i_p \in (0^\circ, 180^\circ)$ is the inclination of the pulsar spin to the line of sight, $\theta \in (0^\circ, 90^\circ)$ is the angle between the magnetic dipole and the spin axis, and $\phi_p \in (0, 1)$ is the phase when the northern magnetic pole is closest to the observer.

Considering the rather different PA phase dependence in both observations, we first applied this model to each observation separately using the same Markov chain Monte Carlo (MCMC) procedure as in Doroshenko et al. (2022) directly fitting observed PA values in individual phase bins. The best-fit model to the PA data is depicted with the dashed curves in Fig. 2e. The corner plots (Foreman-Mackey 2016) characterizing interdependence of model parameters and showing their best-fit values are presented in Fig. 3. The agreement of the best-fit model with the data is striking particularly for the second observation where the data quality is the best among all pulsars observed to date by IXPE. Indeed, there are only minor residuals around phase 0.6 corresponding to minimal PD values and thus having the lowest significance.

On the other hand, direct comparison of the obtained RVM parameters for the two observations implies significantly different pulsar geometry, which is not really expected. First, we see a rather dramatic change in the pulsar position angle χ_p by roughly 90° . This change might not mean that the pulsar has turned by 90° on the sky, but this could result from the polarization mode switch from X to O or vice versa. Second, there appears also to be a large change in the pulsar inclination i_p , which varies from 50° – 70° in the first observation to about 100° in the second one. The apparent change in χ_p value is also accompanied by the change of zero phase ϕ_p by half a period. Finally, the magnetic obliquity

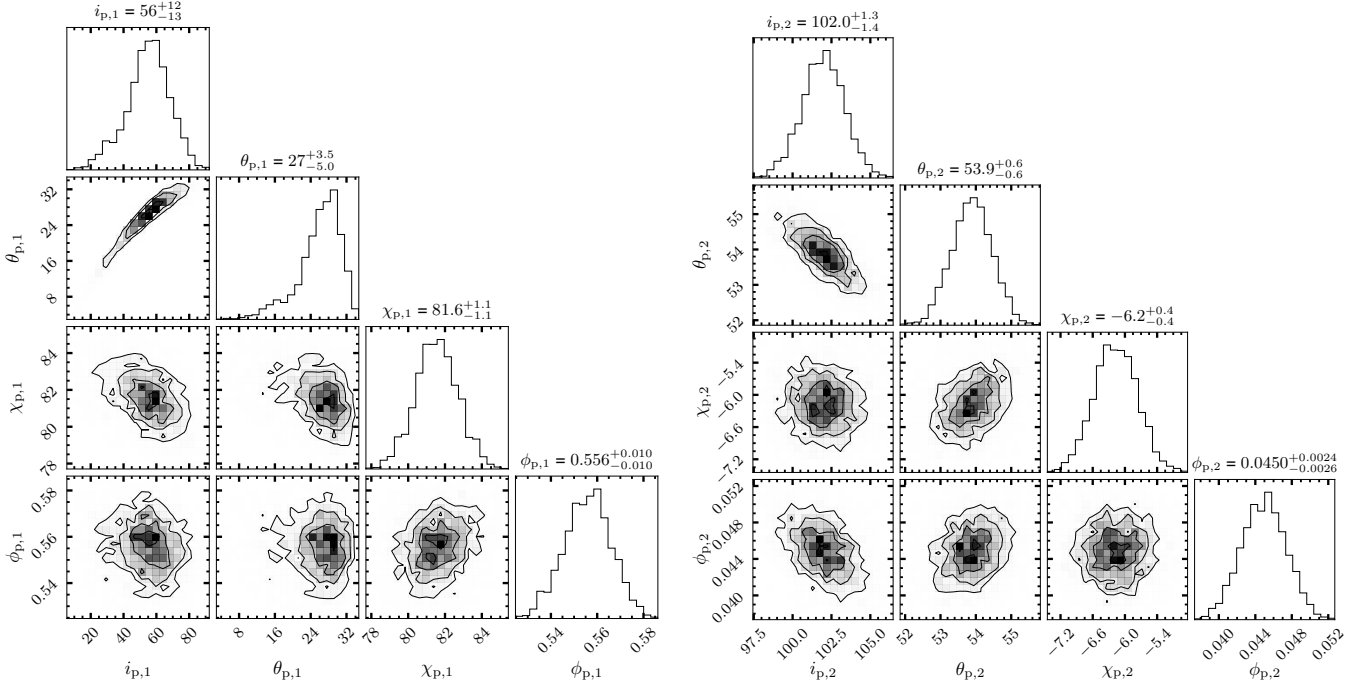


Fig. 3. Corner plots for the RVM fit for each observation individually without additional components. The results for observation 1 (left) and 2 (right) are shown. RVM parameters i_p , θ , and χ_p are in degrees.

θ_p has changed from $\sim 30^\circ$ to $\sim 54^\circ$. While the transition from super- to sub-critical accretion regime (Salganik et al. 2023a) could be expected to lead to a switch of the dominant polarization mode, it does not explain the observed significant changes in other angles. We emphasize that the fact that the observed PA variations are well described by a RVM implies that PA is defined by the magnetic field structure at the polarization radius (Doroshenko et al. 2022) and thus is likely not related to local changes of emission region geometry. On the other hand, it is, of course, difficult to imagine the orientation of the neutron star changing on such a short timescale, and, moreover, time resolved analysis similar to that described above revealed no significant geometry changes within either observation. We considered, therefore, an alternative explanation to the very peculiar behavior of the PA.

4.2. Two-component polarization model

Given the observed changes in the spectral hardness (Salganik et al. 2023a) and pulse profiles, potential presence of an additional polarization component with different properties in one or both observations could be considered as a natural explanation. We attempted, therefore, to single out this component using the spectro-polarimetric analysis of IXPE data. We found, however, that the results are unfortunately inconclusive. That is mainly due to the fact that the available 2–8 keV spectra do not allow one to disentangle reliably the broad continuum components reported by Salganik et al. (2023a), which necessitates broadband spectro-polarimetric analysis to get meaningful results. However, some estimates can be obtained even by using IXPE binned products alone as we discuss below.

Plotting Stokes parameters on the (q, u) -plane, we realized that there is certain similarity between the two observations, but the amplitude of variations is larger in the second observation and the data points are shifted relative to each other. This supports the idea that, in addition to the polarized radiation coming from

the pulsar directly, there is a component that does not depend on phase (or at least less so than the variable pulsar component). A similar conclusion could be reached if one considers the “off-pulse” as background in both observations (i.e. resulting in a more similar phase dependence for both PD and PA). We attempted, therefore, to disentangle the two components through modeling of the observed Stokes parameters. This can be done by expressing the absolute Stokes parameters for each observation as a sum of the variable component described by the RVM and an additional constant component:

$$\begin{aligned} I(\phi) &= I_c + I_p(\phi), \\ Q(\phi) &= Q_c + P_p(\phi)I_p(\phi)\cos[2\chi(\phi)], \\ U(\phi) &= U_c + P_p(\phi)I_p(\phi)\sin[2\chi(\phi)]. \end{aligned} \quad (2)$$

By I , Q and U we can assume here the observed Stokes parameters normalized to the average flux value with indices denoting the constant (c) and pulsed (p) components, P_p is the PD of the variable component, and its PA χ is given by Eq. (1). The Stokes parameters (Q_c , U_c) are related to the PD, P_c , and the flux, I_c , of the constant component:

$$Q_c = P_c I_c \cos(2\chi_c), \quad U_c = P_c I_c \sin(2\chi_c), \quad (3)$$

with its PA being $\chi_c = (1/2) \arctan(U_c/Q_c)$. The polarized flux of the variable component is computed as

$$P_p I_p(\phi) = \sqrt{[Q(\phi) - Q_c]^2 + [U(\phi) - U_c]^2}. \quad (4)$$

The expected PD and PA of the total emission can then be obtained from the summed Stokes parameters of both components and can be compared with the observed values. The null hypothesis is now that the geometry of the pulsar does not change between the observations and the observed changes in the polarization properties are related to presence of an additional unpulsed polarized component. This means that a single RVM could fit

the variable $PA(\phi)$ for both observations. In practice this can be done by including six additional parameters ($I_{c,i}, Q_{c,i}, U_{c,i}$) corresponding to the Stokes parameters (normalized to the average flux) of the constant component in two observations ($i = 1, 2$) in the model so that the right part of Eq. (2) is fully defined. The four RVM parameters and ($I_{c,i}, Q_{c,i}, U_{c,i}$) can then be estimated by comparing the model prediction with the observed Q, U values. Note that in this case modeling is done directly in Q, U space, i.e. observed PA/PD values are not used directly. To obtain model parameters and their uncertainties, we used MCMC sampling as implemented in the `emcee` package (Foreman-Mackey et al. 2013) assuming uniform priors for all parameters except for i_p and θ where flat priors for cosine of the angles were assumed. The likelihood was calculated using χ^2 statistics for Q, U (as the uncertainties of the observed Stokes parameters are normally distributed), and set to negative infinity for parameters outside of ranges defined above for the RVM and for $P_c > 1$ and $P_p(\phi) > 1$ to account for prior knowledge of their possible values. The results are presented in Figs. 4 and 5.

We emphasize the main role in the analysis above is played by the Stokes parameters Q_c, U_c (normalized to the averaged flux) of the constant component. The obtained RVM parameters $i_p = 108^\circ \pm 2^\circ$, $\theta = 48^\circ \pm 1^\circ$, $\chi_p = -8.4 \pm 0.6$ and $\phi_p = 0.041 \pm 0.002$ do not depend at all on the assumption about I_c and are well constrained within the framework of the adopted two-component polarization model. From the best-fit Stokes parameters of the constant component of $Q_{c,1} = -3.7\% \pm 0.3\%$, $U_{c,1} = 2.6\% \pm 0.3\%$, and $Q_{c,2} = -2.0\% \pm 0.4\%$, $U_{c,2} = 2.1\% \pm 0.4\%$, we can get its PAs $\chi_{c,1} = 72^\circ \pm 2^\circ$ and $\chi_{c,2} = 67^\circ \pm 4^\circ$ and the polarized fluxes $P_{c,i} I_{c,i} = \sqrt{Q_{c,i}^2 + U_{c,i}^2}$ of $4.5\% \pm 0.3\%$ and $2.9\% \pm 0.4\%$ for the two observations, respectively. The data allow us to constrain the polarized flux of the constant component, whereas the flux and the PD separately cannot be well determined. The limits on $I_{c,i}$ only appear because the PDs of both components, P_c and P_p , need to be less than 100%. This condition translates to the limits on the flux of the constant component, $I_c \geq P_c I_c$ and $I_c \leq \min[I(\phi) - P_p(\phi)I_p(\phi)]$, as is apparent in Fig. 5. The resulting limits are $I_{c,1} \in [0.038, 0.42]$ for the first and $I_{c,2} \in [0.013, 0.44]$ for the second observation. For the maximum possible I_c , we get minimum possible $P_{c,1} \approx 12\%$ and $P_{c,2} \approx 7\%$, and P_c grows inversely proportional to I_c . For example, for the mean $I_c = 0.23$ we get $P_{c,1} \approx 20\%$ and $P_{c,2} \approx 12.5\%$.

These estimates are relevant for discussion of the physical origin of constant component. Indeed, to remain independent of the pulse phase, the constant component must originate far from the neutron star. Possible sites include reprocessing in the matter piled up at the magnetosphere, reflection from the accretion disk or in disk winds, scattering in the circumbinary disk of the Be star, or reprocessing in the atmosphere of the donor star itself. The fraction of reprocessed light is, however, of the order of 20%, i.e. relatively high, so the origin of the component must be able to explain it, which favors locations relatively close to the pulsar, e.g. the magnetosphere and/or accretion disk. Considering the growing evidence for presence of outflows launched from inner regions of the accretion disk of BeXRBs during both Type II and Type I outbursts (Jaisawal et al. 2019; van den Eijnden et al. 2019, 2022; Chatzis et al. 2022; van den Eijnden et al. 2022) and an expected non-negligible effect on pulse profiles and spectra at higher accretion rates (Mushtukov & Portegies Zwart 2023), scattering in a highly ionized equatorial disk wind seems to be a plausible scenario. Reprocessing in the inner disk regions and disk wind have also been suggested to be responsible for the soft excess observed in many transient X-ray pulsars

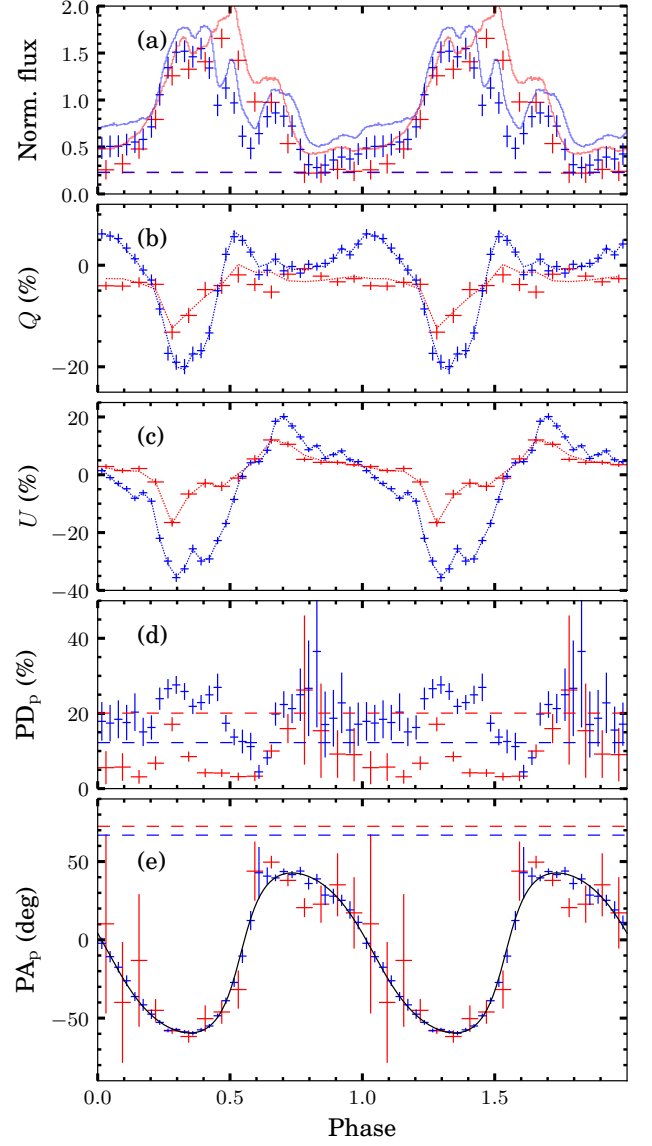


Fig. 4. Results for the two-component model corresponding to the best-fit parameters listed in Fig. 5. Panel (a) shows the total normalized flux (solid lines), the mean value for the constant component ($I_{c,1} = I_{c,2} = 0.23$, dashed horizontal lines), and the flux of the variable component accounting for the uncertainty in the constant component (crosses). Panels (b) and (c) show the observed Stokes parameters normalized to the average flux (crosses) and the best-fit model (dotted lines). Panels (d) and (e) show the PD and PA for constant (dashed horizontal lines) and variable (crosses) components. The solid line in panel (e) matches the solid set of lines in Fig. 2e with the constant component subtracted. Red and blue symbols and lines correspond to observations 1 and 2, respectively.

(Hickox et al. 2004) including RX J0440.9+4431 (Salganik et al. 2023a) for which the soft excess was also found to be more prominent at higher luminosities. Larger deviations from the RVM and the higher PD of the constant component in the first observation, where the accretion rate and likely the outflow rate were higher, is also in line with this hypothesis. For an idealized case when the scattering material lies in a plane, the polarization of the scattered component depends on the inclination to the plane normal i as $PD = \sin^2 i / (3 - \cos^2 i)$ (Sunyaev & Titarchuk 1985), reaching 33% edge-on and is still larger than 30% for

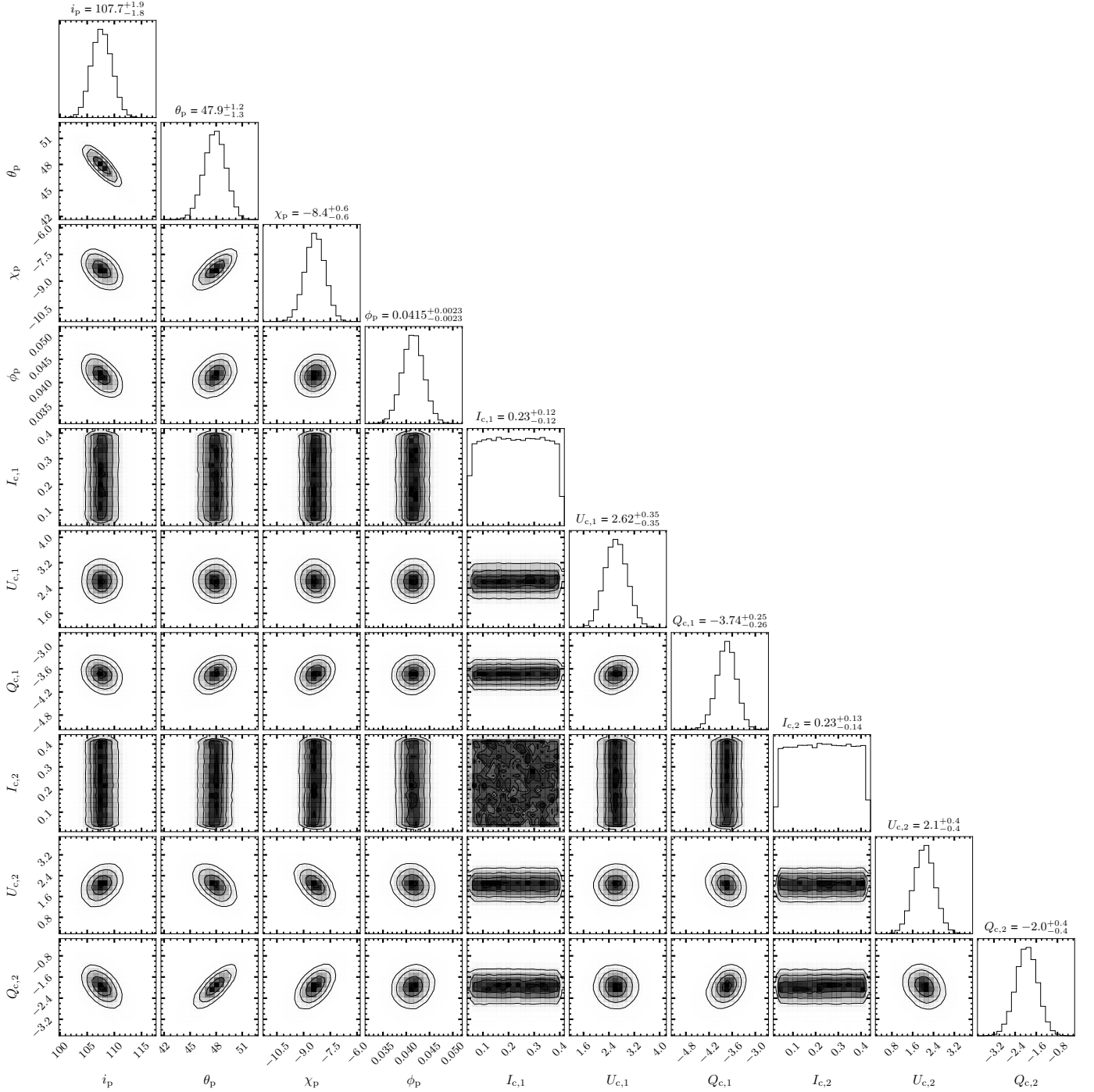


Fig. 5. Corner plots for the simultaneous fit of both observations including the unpulsed polarization component contribution (parameters correspond to a set of solid lines in Fig. 2e and lines in Fig. 4). The RVM parameters i_p , θ , and χ_p are in degrees. The Stokes parameters $Q_{c,i}$ and $U_{c,i}$ are expressed in percents of the average flux, while $I_{c,i}$ are fractions of the average flux. The uncertainties are reported at 1σ confidence level.

$i > 66^\circ$. For a wind occupying a larger solid angle, the PD drops, but even for the half-opening of the wind (measured from the orbital plane) of 30° (i.e. occupying half of the sky as seen from the pulsar), the PD drops just by a factor of 0.77 being above 22% for $i > 66^\circ$. These estimates of the PD are comparable to the data. The contribution of the scattered emission to the total flux in the soft band can also be appreciable, reaching tens of percent at least at higher accretion rates (Jaisawal et al. 2019). More accurate constraints on the fraction of scattered light and polarization of the scattered component can also be obtained

through broadband spectral analysis and detailed modeling of scattering and fluorescent lines in vicinity of the pulsar.

We note also that a high estimated value of pulsar inclination suggests that the accretion disk is likely viewed close to edge-on, which is expected to yield the largest polarization. We note that in this scenario the PA of the constant component is expected to be aligned with the position angle of the normal to the accretion disk and the orbital plane, and thus not expected to change with the orbital phase which is consistent with observations. Orientation of the accretion disk relative to the decretion disk of the Be star

can be tested through optical polarimetric observations. Preliminary analysis of data obtained as part of our optical polarimetric campaign with the DIPol-2 high-precision polarimeter (Pirola et al. 2014) at the T60 telescope at Haleakala observatory yields the PA of the intrinsic optical polarization of $55^\circ\text{--}71^\circ$ (Nitindala A. P. et al., in prep.). Such a close agreement with the X-ray PA does not look like a coincidence, and probably implies that the pulsar orbit lies close to the decretion disk plane.

It is interesting to discuss the phase dependence of the variable component. First, one can note that $\phi_p = 0$ corresponds to the northern pole coming close to the observer, while at $\phi_p = 0.5$ the southern pole is close. For the estimated $i_p = 108^\circ$ and $\theta = 48^\circ$, the minimum angles between the normal to the spots and the line of sight are $i_p - \theta = 60^\circ$ and $180^\circ - \theta - i_p = 24^\circ$, respectively. So it is not surprising that flux has a maximum when the southern spot is closer to observer in both observations.

5. Summary and conclusions

We presented the first results of IXPE observations of the 2023 Type II outburst of a bright Be transient RX J0440.9+4431. The observations were carried out at two luminosity levels and likely captured the object in two accretion regimes associated with the presence and the absence of an accretion column (Basko & Sunyaev 1976; Salganik et al. 2023a). This presents a unique opportunity to probe the changes in emission region geometry and radiative processes related to onset of an accretion column by means of pulse-phase resolved X-ray polarimetry.

Our analysis indeed revealed that the source is strongly polarized in both observations with the PD exceeding 20% in some phase bins. The observed PA phase dependence remains remarkably consistent with the predictions from the RVM model (Radhakrishnan & Cooke 1969; Poutanen 2020) but the derived geometrical parameters appear to be completely different for the two observations. While the observed 90° jump in the pulsar spin position angle could be attributed to a change in the dominant polarization mode associated with the transition, there is no obvious explanation for changes in other angles which amount to tens of degrees on a timescale of just a few days. It is difficult to imagine that such changes are associated with a true change of the orientation of the neutron star's spin and magnetic axes with respect to the observer. That led us to consider alternative explanations, in particular, a potential presence of an additional polarized component.

We find that the observed PA phase dependence in both observations can indeed be described with no changes in pulsar geometry if a strongly polarized (PD \sim 10–30%, PA \approx 70°) unpulsed component is present. Subtracting the Stokes parameters of the constant component from the observed ones, we have derived constraints on the pulsar geometry, obtaining a pulsar inclination of $i_p \approx 108^\circ$, a magnetic obliquity of $\theta \approx 48^\circ$ and a position angle of the pulsar spin of $\chi_p \approx -8.4^\circ$. Properties of the unpulsed component (e.g. its contribution to the total flux, the PD and PA) appear to be roughly constant between the two observations. We suggest that this component can be produced by scattering of the pulsar radiation in a highly ionized disk wind. The observed PA phase dependence is consistent, and for the second observation shows almost perfect agreement, with the simple RVM model used up to now to study the geometry of XRP. Yet, despite formal agreement, more detailed analysis of the two observations carried out at different epochs reveals that the situation is way more complicated. We conclude, therefore, that the importance of multi-epoch high quality polarimetric observations, preferably ac-

companied by broadband spectroscopic and optical polarimetric observations, should not be underestimated.

Acknowledgements. The Imaging X-ray Polarimetry Explorer (IXPE) is a joint US and Italian mission. The US contribution is supported by the National Aeronautics and Space Administration (NASA) and led and managed by its Marshall Space Flight Center (MSFC), with industry partner Ball Aerospace (contract NNM15AA18C). The Italian contribution is supported by the Italian Space Agency (Agenzia Spaziale Italiana, ASI) through contract ASI-OHBI-2017-12-I.0, agreements ASI-INAF-2017-12-H0 and ASI-INFN-2017.13-H0, and its Space Science Data Center (SSDC) with agreements ASI-INAF-2022-14-HH.0 and ASI-INFN 2021-43-HH.0, and by the Istituto Nazionale di Astrofisica (INAF) and the Istituto Nazionale di Fisica Nucleare (INFN) in Italy. This research used data products provided by the IXPE Team (MSFC, SSDC, INAF, and INFN) and distributed with additional software tools by the High-Energy Astrophysics Science Archive Research Center (HEASARC), at NASA Goddard Space Flight Center (GSFC). We acknowledge support from the German Academic Exchange Service (DAAD) travel grant 57525212 (VD, VFS), the Academy of Finland grants 333112, 349144, 349373, and 349906 (JP, SST, SVF), the Natural Sciences and Engineering Research Council of Canada (NSERC) and the Canadian Space Agency (JH), the Väisälä Foundation (SST), UKRI Stephen Hawking fellowship (AAM), the German Research Foundation (DFG) grant WE 1312/59-1 (VFS), the Vilho, Yrjö and Kalle Väisälä Foundation, and Suomen Kulttuurirahasto (VK).

References

- Arnaud, K. A. 1996, in ASP Conf. Ser., Vol. 101, *Astronomical Data Analysis Software and Systems V*, ed. G. H. Jacoby & J. Barnes (San Francisco: Astron. Soc. Pac.), 17–20
- Bailer-Jones, C. A. L., Rybizki, J., Fouesneau, M., Demleitner, M., & Andrae, R. 2021, *AJ*, 161, 147
- Baldini, L., Barbanera, M., Bellazzini, R., et al. 2021, *Astroparticle Physics*, 133, 102628
- Baldini, L., Bucciantini, N., Di Lalla, N., et al. 2022, *SoftwareX*, 19, 101194
- Basko, M. M. & Sunyaev, R. A. 1976, *MNRAS*, 175, 395
- Chatzis, M., Petropoulou, M., & Vasilopoulos, G. 2022, *MNRAS*, 509, 2532
- Coley, J. B., Gendreau, K., Pottschmidt, K., et al. 2023, *The Astronomer's Telegram*, 15907, 1
- Deeter, J. E., Boynton, P. E., & Pravdo, S. H. 1981, *ApJ*, 247, 1003
- Di Marco, A., Soffitta, P., Costa, E., et al. 2023, *AJ*, 165, 143
- Doroshenko, V., Poutanen, J., Tsygankov, S. S., et al. 2022, *Nature Astronomy*, 6, 1433
- Doroshenko, V., Zhang, S. N., Santangelo, A., et al. 2020, *MNRAS*, 491, 1857
- Ferrigno, C., Farinelli, R., Bozzo, E., et al. 2013, *A&A*, 553, A103
- Finger, M. H. & Camero-Aranz, A. 2010, *The Astronomer's Telegram*, 2537, 1
- Foreman-Mackey, D. 2016, *The Journal of Open Source Software*, 1, 24
- Foreman-Mackey, D., Hogg, D. W., Lang, D., & Goodman, J. 2013, *PASP*, 125, 306
- Forsblom, S. V., Poutanen, J., Tsygankov, S. S., et al. 2023, *ApJ*, 947, L20
- Gnedin, Y. N., Pavlov, G. G., & Shibano, Y. A. 1978, *Soviet Astronomy Letters*, 4, 117
- González-Caniulef, D., Caiazzo, I., & Heyl, J. 2023, *MNRAS*, 519, 5902
- Heyl, J. S. & Shaviv, N. J. 2000, *MNRAS*, 311, 555
- Hickox, R. C., Narayan, R., & Kallman, T. R. 2004, *ApJ*, 614, 881
- Jaisawal, G. K., Wilson-Hodge, C. A., Fabian, A. C., et al. 2019, *ApJ*, 885, 18
- Kislat, F., Beilicke, M., Guo, Q., Zajczyk, A., & Krawczynski, H. 2015, *Astroparticle Physics*, 64, 40
- La Palombara, N., Sidoli, L., Esposito, P., Tiengo, A., & Mereghetti, S. 2012, *A&A*, 539, A82
- Malacaria, C., Heyl, J., Doroshenko, V., et al. 2023, *A&A*, in press, arXiv:2304.00925
- Malacaria, C., Jenke, P., Roberts, O. J., et al. 2020, *ApJ*, 896, 90
- Morii, M., Kawai, N., Sugimori, K., et al. 2010, *The Astronomer's Telegram*, 2527, 1
- Motch, C., Haberl, F., Dennerl, K., Pakull, M., & Janot-Pacheco, E. 1997, *A&A*, 323, 853
- Mushtukov, A. A. & Portegies Zwart, S. 2023, *MNRAS*, 518, 5457
- Mushtukov, A. A., Tsygankov, S. S., Poutanen, J., et al. 2023, *MNRAS*, submitted, arXiv:2303.17325
- Nakajima, M., Negoro, H., Mihara, T., et al. 2022, *The Astronomer's Telegram*, 15835, 1
- Pal, S., Mandal, M., Gendreau, K., et al. 2023, *The Astronomer's Telegram*, 15868, 1
- Pavlov, G. G. & Shibano, Y. A. 1979, *Soviet Journal of Experimental and Theoretical Physics*, 49, 741
- Pirola, V., Berdyugin, A., & Berdyugina, S. 2014, in *Proc. SPIE*, Vol. 9147, *Ground-based and Airborne Instrumentation for Astronomy V*, 91478I

- Poutanen, J. 2020, *A&A*, 641, A166
- Radhakrishnan, V. & Cooke, D. J. 1969, *Astrophys. Lett.*, 3, 225
- Reig, P., Negueruela, I., Fabregat, J., Chato, R., & Coe, M. J. 2005, *A&A*, 440, 1079
- Reig, P. & Nespoli, E. 2013, *A&A*, 551, A1
- Reig, P. & Roche, P. 1999, *MNRAS*, 306, 100
- Salganik, A., Tsygankov, S. S., Doroshenko, V., et al. 2023a, *MNRAS*, submitted, arXiv:2304.14881
- Salganik, A., Tsygankov, S. S., Lutovinov, A. A., & Molkov, S. V. 2023b, *The Astronomer's Telegram*, 15874, 1
- Soffitta, P., Baldini, L., Bellazzini, R., et al. 2021, *AJ*, 162, 208
- Sunyaev, R. A. & Titarchuk, L. G. 1985, *A&A*, 143, 374
- Tsygankov, S. S., Doroshenko, V., Mushtukov, A. A., et al. 2023, *A&A*, in press, arXiv:2302.06680
- Tsygankov, S. S., Doroshenko, V., Poutanen, J., et al. 2022, *ApJ*, 941, L14
- Tsygankov, S. S., Krivonos, R. A., & Lutovinov, A. A. 2012, *MNRAS*, 421, 2407
- Tsygankov, S. S., Mushtukov, A. A., Suleimanov, V. F., et al. 2017, *A&A*, 608, A17
- Usui, R., Morii, M., Kawai, N., et al. 2012, *PASJ*, 64, 79
- van den Eijnden, J., Degenaar, N., Russell, T. D., et al. 2022, *MNRAS*, 516, 4844
- van den Eijnden, J., Degenaar, N., Schulz, N. S., et al. 2019, *MNRAS*, 487, 4355
- Weisskopf, M. C., Soffitta, P., Baldini, L., et al. 2022, *JATIS*, 8, 026002
- Wilson-Hodge, C. A., Malacaria, C., Jenke, P. A., et al. 2018, *ApJ*, 863, 9
- ¹ Institut für Astronomie und Astrophysik, Universität Tübingen, Sand 1, D-72076 Tübingen, Germany e-mail: doroshv@astro.uni-tuebingen.de
- ² Department of Physics and Astronomy, FI-20014 University of Turku, Finland
- ³ University of British Columbia, Vancouver, BC V6T 1Z4, Canada
- ⁴ Division of Physics, Mathematics and Astronomy, California Institute of Technology, Pasadena, CA 91125, USA
- ⁵ Dipartimento di Fisica e Astronomia, Università degli Studi di Padova, Via Marzolo 8, 35131 Padova, Italy
- ⁶ Mullard Space Science Laboratory, University College London, Holmbury St Mary, Dorking, Surrey RH5 6NT, UK
- ⁷ Nordita, KTH Royal Institute of Technology and Stockholm University, Hannes Alfvéns väg 12, SE-106 91 Stockholm, Sweden
- ⁸ NASA Marshall Space Flight Center, Huntsville, AL 35812, USA
- ⁹ Institut de Recherche en Astrophysique et Planétologie, UPS-OMP, CNRS, CNES, 9 avenue du Colonel Roche, BP 44346 31028, Toulouse CEDEX 4, France
- ¹⁰ International Space Science Institute, Hallerstrasse 6, 3012 Bern, Switzerland
- ¹¹ Astrophysics, Department of Physics, University of Oxford, Denys Wilkinson Building, Keble Road, Oxford OX1 3RH, UK
- ¹² Space Research Institute (IKI) of the Russian Academy of Sciences, Profsoyuznaya Str. 84/32, Moscow 117997, Russia
- ¹³ Department of Astrophysics, St. Petersburg State University, Universitetskyy pr. 28, Petrodvorets, 198504 St. Petersburg, Russia
- ¹⁴ Instituto de Astrofísica de Andalucía – CSIC, Glorieta de la Astronomía s/n, 18008 Granada, Spain
- ¹⁵ INAF Osservatorio Astronomico di Roma, Via Frascati 33, 00040 Monte Porzio Catone (RM), Italy
- ¹⁶ Space Science Data Center, Agenzia Spaziale Italiana, Via del Politecnico snc, 00133 Roma, Italy
- ¹⁷ INAF Osservatorio Astronomico di Cagliari, Via della Scienza 5, 09047 Selargius (CA), Italy
- ¹⁸ Istituto Nazionale di Fisica Nucleare, Sezione di Pisa, Largo B. Pontecorvo 3, 56127 Pisa, Italy
- ¹⁹ Dipartimento di Fisica, Università di Pisa, Largo B. Pontecorvo 3, 56127 Pisa, Italy
- ²⁰ Dipartimento di Matematica e Fisica, Università degli Studi Roma Tre, via della Vasca Navale 84, 00146 Roma, Italy
- ²¹ Istituto Nazionale di Fisica Nucleare, Sezione di Torino, Via Pietro Giuria 1, 10125 Torino, Italy
- ²² Dipartimento di Fisica, Università degli Studi di Torino, Via Pietro Giuria 1, 10125 Torino, Italy
- ²³ INAF Osservatorio Astrofisico di Arcetri, Largo Enrico Fermi 5, 50125 Firenze, Italy
- ²⁴ Dipartimento di Fisica e Astronomia, Università degli Studi di Firenze, Via Sansone 1, 50019 Sesto Fiorentino (FI), Italy
- ²⁵ Istituto Nazionale di Fisica Nucleare, Sezione di Firenze, Via Sansone 1, 50019 Sesto Fiorentino (FI), Italy
- ²⁶ Agenzia Spaziale Italiana, Via del Politecnico snc, 00133 Roma, Italy
- ²⁷ Science and Technology Institute, Universities Space Research Association, Huntsville, AL 35805, USA
- ²⁸ Istituto Nazionale di Fisica Nucleare, Sezione di Roma “Tor Vergata”, Via della Ricerca Scientifica 1, 00133 Roma, Italy
- ²⁹ INAF Istituto di Astrofisica e Planetologia Spaziali, Via del Fosso del Cavaliere 100, 00133 Roma, Italy
- ³⁰ Department of Physics and Kavli Institute for Particle Astrophysics and Cosmology, Stanford University, Stanford, California 94305, USA
- ³¹ Astronomical Institute of the Czech Academy of Sciences, Boční II 1401/1, 14100 Praha 4, Czech Republic
- ³² RIKEN Cluster for Pioneering Research, 2-1 Hirosawa, Wako, Saitama 351-0198, Japan
- ³³ California Institute of Technology, Pasadena, CA 91125, USA
- ³⁴ Yamagata University, 1-4-12 Kojirakawa-machi, Yamagata-shi 990-8560, Japan
- ³⁵ Osaka University, 1-1 Yamadaoka, Suita, Osaka 565-0871, Japan
- ³⁶ International Center for Hadron Astrophysics, Chiba University, Chiba 263-8522, Japan
- ³⁷ Institute for Astrophysical Research, Boston University, 725 Commonwealth Avenue, Boston, MA 02215, USA
- ³⁸ Department of Physics and Astronomy and Space Science Center, University of New Hampshire, Durham, NH 03824, USA
- ³⁹ Physics Department and McDonnell Center for the Space Sciences, Washington University in St. Louis, St. Louis, MO 63130, USA
- ⁴⁰ Finnish Centre for Astronomy with ESO, 20014 University of Turku, Finland
- ⁴¹ Istituto Nazionale di Fisica Nucleare, Sezione di Napoli, Strada Comunale Cinthia, 80126 Napoli, Italy
- ⁴² Université de Strasbourg, CNRS, Observatoire Astronomique de Strasbourg, UMR 7550, 67000 Strasbourg, France
- ⁴³ MIT Kavli Institute for Astrophysics and Space Research, Massachusetts Institute of Technology, 77 Massachusetts Avenue, Cambridge, MA 02139, USA
- ⁴⁴ Graduate School of Science, Division of Particle and Astrophysical Science, Nagoya University, Furo-cho, Chikusa-ku, Nagoya, Aichi 464-8602, Japan
- ⁴⁵ Hiroshima Astrophysical Science Center, Hiroshima University, 1-3-1 Kagamiyama, Higashi-Hiroshima, Hiroshima 739-8526, Japan
- ⁴⁶ University of Maryland, Baltimore County, Baltimore, MD 21250, USA
- ⁴⁷ NASA Goddard Space Flight Center, Greenbelt, MD 20771, USA
- ⁴⁸ Center for Research and Exploration in Space Science and Technology, NASA/GSFC, Greenbelt, MD 20771, USA
- ⁴⁹ Department of Physics, University of Hong Kong, Pokfulam, Hong Kong
- ⁵⁰ Department of Astronomy and Astrophysics, Pennsylvania State University, University Park, PA 16801, USA
- ⁵¹ Université Grenoble Alpes, CNRS, IPAG, 38000 Grenoble, France
- ⁵² Center for Astrophysics, Harvard & Smithsonian, 60 Garden St, Cambridge, MA 02138, USA
- ⁵³ INAF Osservatorio Astronomico di Brera, via E. Bianchi 46, 23807 Merate (LC), Italy
- ⁵⁴ Dipartimento di Fisica, Università degli Studi di Roma “Tor Vergata”, Via della Ricerca Scientifica 1, 00133 Roma, Italy
- ⁵⁵ Department of Astronomy, University of Maryland, College Park, Maryland 20742, USA
- ⁵⁶ Anton Pannekoek Institute for Astronomy & GRAPPA, University of Amsterdam, Science Park 904, 1098 XH Amsterdam, The Netherlands
- ⁵⁷ Guangxi Key Laboratory for Relativistic Astrophysics, School of Physical Science and Technology, Guangxi University, Nanning 530004, China